Asymmetric Behavior of an Oceanic Boundary Layer above a Sloping Bottom*

J. H. TROWBRIDGE AND S. J. LENTZ

Woods Hole Oceanographic Institution, Woods Hole, Massachusetts

(Manuscript received 13 July 1990, in final form 19 February 1991)

ABSTRACT

The effects of stratification, planetary rotation and a sloping bottom combine to produce an asymmetric response in which the characteristics of an oceanic bottom boundary layer depend on the direction, in addition to the magnitude, of the along-isobath velocity in the inviscid interior. The asymmetric response is examined theoretically under idealized conditions in which the motion begins from rest, the flow is uniform in the along-isobath and cross-isobath directions, and the water column is initially uniformly stratified. The analysis is based on an integrated model, in which the bottom stress is determined from a quadratic drag law, and the height of the boundary layer is determined from a Pollard–Rhines–Thompson mixing criterion. The model indicates rapid mixing at the onset of forcing to a height limited by planetary rotation and interior stratification, followed by evolution in which the height of the boundary layer may either increase or remain fixed near its initial value, depending on the behavior of the buoyancy within the boundary layer and the shear across the top of the layer. The model indicates reduction of the velocity within the boundary layer with increasing time, as a result of increasingly important buoyancy forces acting in opposition to the forcing by the dynamic pressure gradient. Model results compare favorably with previous turbulence closure computations, and the model reproduces the qualitative asymmetric behavior apparent in observations of boundary layer height.

1. Introduction

Lentz and Trowbridge (1991) recently reported estimates of the height and structure of the bottom mixed layer over the continental shelf off northern California, based on measurements obtained during the Coastal Ocean Dynamics Experiment (CODE). The bottom mixed layer varied in height between a few meters and a few tens of meters, and was typically overlain by a stably stratified interior. The height of the mixed layer varied with the interior stratification and with the magnitude of the predominantly along-isobath interior velocity. A much clearer and more unexpected feature, however, was an asymmetric response in which the height of the mixed layer depended on the direction of the interior velocity, in addition to its magnitude. For flows of comparable strength, bottom mixed layers were thicker during downwelling-favorable flows, and thinner during upwelling-favorable flows (see Fig. 1). The purpose of this paper is to examine analytically, in as simple a manner as possible, the observed asymmetric response of the bottom mixed layer to forcing by the interior flow.

Similar dependence of mixed layer height on flow direction has been observed previously (Weatherly and Niiler 1974; Eittreim et al. 1975), and a possible explanation is cross-isobath Ekman transport of buoyancy over a sloping bottom (Weatherly and Niiler 1974; Weatherly 1975; Weatherly and Martin 1978). During upwelling, the Ekman transport within the bottom boundary layer advects dense water upslope, increasing the density difference between the boundary layer and the interior, so that vertical turbulent transport near the top of the layer is suppressed and the growth of the layer is inhibited. During downwelling, the Ekman transport within the boundary layer advects light water downslope, reducing the density difference between the boundary layer and the interior, so that vertical turbulent transport and the growth of the layer are enhanced.

We present in this paper an analysis that addresses the influence of bottom slope on the height and structure of a stably stratified, rotating bottom boundary layer. The analysis treats an idealized problem in which a boundary layer mixes vertically into an initially uniformly stratified water column over a gently sloping, perfectly insulating sea floor. The interior velocity is spatially uniform and parallel to the isobaths, and the Ekman transport within the boundary layer advects dense water upslope or light water downslope, depending on the direction of the interior flow.

The problem addressed in this paper was studied earlier by Weatherly (1975), Weatherly and Martin (1978), and Bird et al. (1982), based on gradient transport models in which the effective diffusivities

* Contribution Number 7456 from the Woods Hole Oceanographic Institution.

Corresponding author address: Dr. Steven Lentz, Woods Hole Oceanographic Institution, Woods Hole, MA 02543.

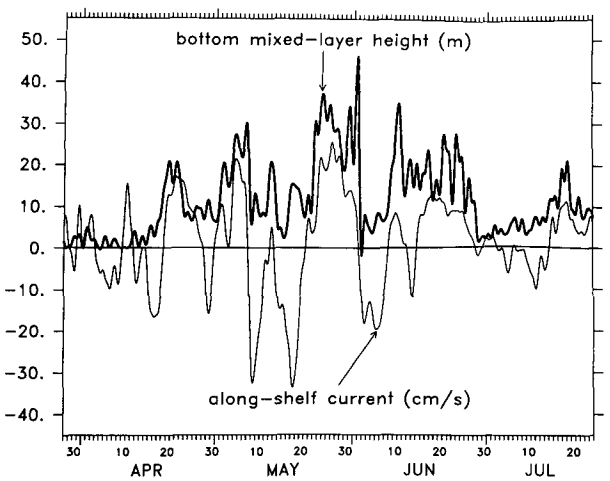

FIG. 1. Measurements from the CODE C3 site, at a depth of 90 m. The light line is the along-isobath velocity 37 m above bottom in cm s^{-1}, and the heavy line is the Lentz and Trowbridge estimate of the height of the bottom mixed layer in m, based on temperature measurements 1 m, 7 m, 20 m, 37 m and 55 m above bottom. Estimates of mixed layer height (with coarse vertical resolution) were obtained from hourly temperature measurements. Both velocity and mixed layer height are filtered (half-amplitude period of 33 hours). Positive velocity is poleward (downwelling favorable) and negative velocity is equatorward (upwelling favorable). To see the dependence of mixed layer height on flow direction, compare the upwelling-favorable flows centered approximately on 17 April, 29 April, 9 May, 19 May, 5 June and 10 July with the downwelling-favorable flows centered approximately on 23 April, 6 May, 27 May, 20 June and 18 July.

were calculated from detailed turbulence closures. The early studies demonstrated the effect of the bottom slope on the structure of the boundary layer, and illustrated some of the characteristics of the boundary layer at small times, but were limited in scope and interpretation because of the complexity of the approach. A more recent series of related studies (Thorpe 1987; Garrett 1990; MacCready and Rhines 1991) has provided insight into the transient evolution, the role of buoyancy forces, and the effects of the boundary layer on spinup and mixing in the interior. The recent studies do not, however, address the effect of the flow itself on the processes that control the mixing, which is, in our view, an important part of the problem at geophysical scales.

The analysis presented in this paper is much simpler than the early treatments based on turbulence closures, yet includes in a plausible way the effect of the flow itself on the rate of vertical mixing. The analysis is based on an integrated model similar to those used previously by Pollard et al. (1973) and Thompson (1973). In this model, the bottom stress is determined from a quadratic drag law, and the height of the boundary layer is determined from a mixing criterion that limits the bulk Richardson number to values greater than or equal to unity. The integrated model produces results that are consistent with the more detailed computations obtained from turbulence closures, and provides, in addition, qualitative information about the physics, including estimates of time scales and determination of the parameter dependence of the boundary layer behavior.

The remainder of this paper is organized as follows. We formulate the model in section 2 and we present model results in section 3, including a comparison with Weatherly's and Martin's (1978) turbulence closure computations, and an analysis of the response to impulsively imposed forcing. Section 4 is a discussion, and conclusions are summarized in section 5.

2. Model formulation

a. Geometry and governing equations

The problem addressed in this paper is shown schematically in Fig. 2. A semi-infinite fluid domain is bounded below by a gently sloping bottom. Initially, the fluid is at rest, with horizontal isopycnal surfaces and spatially uniform buoyancy frequency. At some initial time, a spatially uniform dynamic pressure gradient is applied to this system, so that the fluid begins to move parallel to the bottom and a turbulent boundary layer forms adjacent to the bottom. In the interior, above the boundary layer, the velocity is spatially uniform, the density gradients are constant and the same as in the initial state, and the turbulent fluxes are zero. In the boundary layer, the ensemble-averaged turbulent fluxes, ensemble-averaged velocity, and ensemble-averaged density anomaly (departure from the interior density) depend only on time and on distance away from the bottom. The interior velocity and density are given, and the problem is to determine the ensemble-averaged velocity and density fields within the boundary layer.

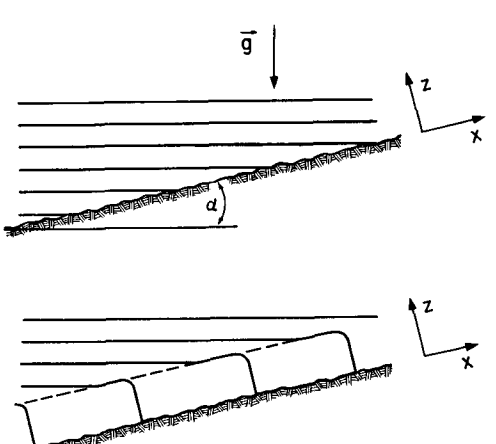

FIG. 2. (a) Geometry in the initial rest state. The solid lines are isopycnal surfaces. Symbols are defined in text. (b) Geometry after onset of motion and formation of a bottom boundary layer. The solid lines are isopycnal surfaces and the dashed line is the top of the boundary layer.

The present analysis is limited to the case of a perfectly insulating sea floor, so that the density flux across the bottom is zero. We assume that molecular fluxes of mass and momentum have a negligible effect on the ensemble-averaged flow field over the time scales of interest in this paper, except possibly in a thin unresolved viscous sublayer adjacent to the bottom. The analysis is limited to cases in which the interior velocity is purely along-isobath, and we consider only the motions with time scales sufficiently long in comparison to the inertial time scale so that temporal accelerations may be neglected relative to Coriolis accelerations.

The flow shown in Fig. 2 is described by the Boussinesq-approximated equations for a Newtonian fluid (e.g., Phillips 1977). Under the stated conditions, the ensemble-averaged cross-isobath and along-isobath momentum equations and the ensemble-averaged equation describing the density reduce to

$$-fv + \frac{\partial}{\partial z}\langle u'w'\rangle = -fv_I - \frac{\alpha g}{\rho_o}(\rho - \rho_I), \quad (1)$$

$$fu + \frac{\partial}{\partial z}\langle v'w'\rangle = 0, \quad (2)$$

$$\frac{\partial}{\partial t}(\rho - \rho_I) = -u\frac{\partial \rho_I}{\partial x} - \frac{\partial}{\partial z}\langle \rho'w'\rangle, \quad (3)$$

(e.g., Weatherly and Martin 1978). Here the coordinate system is defined so that the x–y plane coincides with the bottom, with x across-isobath, y along-isobath and z perpendicular to the bottom. The time is denoted by t. The quantities $(u, v, 0)$ and (u', v', w') are respectively the ensemble-averaged and fluctuating components of the velocity vector in the (x, y, z) coordinate system, the quantities ρ and ρ' are, respectively, the ensemble-averaged and fluctuating components of the density, ρ_o is the constant reference density, g is the magnitude of the gravitational acceleration, f is the Coriolis parameter (taken here to be positive), angular brackets denote ensemble averages, subscript I denotes the interior, and α is the bottom slope, which is assumed to be sufficiently small so that $\sin(\alpha) \approx \alpha$ and $\cos(\alpha) \approx 1$. The interior density gradients $\partial\rho_I/\partial x$ and $\partial\rho_I/\partial z$ are constant. The interior density $\rho_I(x, z, t)$ is understood to be defined for all z, although it does not describe the actual density field within the boundary layer. As stated previously, the velocities u and v, the density anomaly $\rho - \rho_I$, and the turbulent fluxes $\langle u'w'\rangle$, $\langle v'w'\rangle$ and $\langle \rho'w'\rangle$ depend only on z and t.

Equations (1), (2) and (3) are obtained by subtracting the equations describing the interior from the equations describing the boundary layer. The terms on the left sides of the x and y momentum equations (1) and (2) are the Coriolis accelerations and the z-derivatives of the Reynolds shear stresses. The terms on the right side of (1) represent a combination of forcing effects produced by the dynamic pressure gradient and by the departure of the density field from the initial density field. Equations (1) and (2) describe the response of the ensemble-averaged velocity and Reynolds stresses to the instantaneous forcing, and equation (3) describes the evolution of the density anomaly due to cross-isobath advection [the first term on the right side of (3)] and turbulent mixing [the last term in (3)]. The mathematical problem is one-dimensional even though cross-isobath advection is present, because advection enters through the effect of the sloping bottom.

b. *Integrated governing equations and closure*

A set of integrated governing equations is obtained by integrating (1), (2) and (3) with respect to z from the bottom to a point just above the boundary layer, and applying appropriate boundary conditions. In the present case, the bottom boundary condition is the requirement that the density flux $\langle \rho'w'\rangle$ vanish at the sea floor, and the boundary conditions just above the boundary layer are the requirements that the turbulent fluxes, density anomaly $\rho - \rho_I$, and velocity anomalies u and $v - v_I$ vanish in the interior. Additional equations are necessary in order to determine the bottom shear stress and the height of the boundary layer. As stated previously, a quadratic drag law is used to relate the vertically averaged velocity to the bottom shear stress, and a mixing criterion based on the bulk Richardson number is used to determine the height of the boundary layer.

Integration of (1), (2) and (3) with respect to z, application of the appropriate boundary conditions, and introduction of a quadratic drag law yields the following set of integrated equations:

$$fh(\bar{v} - v_I) = C_d\sqrt{\bar{u}^2 + \bar{v}^2}\,\bar{u} + \alpha B, \quad (4)$$

$$f_h\bar{u} = -C_d\sqrt{\bar{u}^2 + \bar{v}^2}\,\bar{v}, \quad (5)$$

$$\frac{dB}{dt} = \alpha N^2 h\bar{u}. \quad (6)$$

Here $h(t)$ is the height of the boundary layer, defined simply to be the distance from the bottom at which the velocity anomaly, density anomaly and turbulent fluxes associated with the boundary layer become negligible. A more precise definition of $h(t)$ is not necessary for our purposes. The quantity C_d is the bottom drag coefficient, assumed for simplicity to be constant, and $\bar{u}$ and $\bar{v}$ are, respectively, the x and y components of the velocity averaged over the thickness of the boundary layer:

$$[\bar{u}(t), \bar{v}(t)] = \frac{1}{h}\int_0^h [u(z, t), v(z, t)]dz. \quad (7)$$

The quantity $B(t)$ is the integrated buoyancy deficit within the boundary layer, defined by

$$B(t) = \frac{g}{\rho_o}\int_0^h (\rho - \rho_I)dz. \quad (8)$$

In (6) we have expressed the interior density gradient $\partial\rho_I/\partial x$ in terms of the spatially uniform buoyancy frequency in the interior, denoted by N.

Following Pollard et al. (1973) and Thompson (1973), we introduce a simple mixing criterion to determine the height $h(t)$. The mixing criterion is based on the bulk Richardson number R_b, defined by

$$R_b = \frac{\Delta\rho}{\rho_o}\frac{gh}{|\Delta\mathbf{u}|^2}. \tag{9}$$

Here $\Delta\rho$ is the difference between the density averaged over the thickness of the boundary layer and the density just above the boundary layer, and $\Delta\mathbf{u}$ is the difference between the velocity vector averaged over the thickness of the boundary layer and the velocity vector above the boundary layer. In the present notation,

$$R_b = \frac{B + \frac{1}{2}N^2h^2}{\bar{u}^2 + (\bar{v} - v_I)^2}. \tag{10}$$

If R_b is greater than unity, we assume that no mixing occurs, so that h remains unchanged. If R_b is less than unity, we assume that h increases instantaneously (in comparison with the time scales of interest in this paper) to a value at which R_b is equal to unity, at which point mixing ceases. This mixing criterion effectively limits R_b to values greater than or equal to unity, so that we have the following constraint:

$$R_b \geq 1. \tag{11}$$

This constraint reflects the idea that the growth of the boundary layer is limited by a balance between the stabilizing effect of stratification [represented in (9) by $\Delta\rho$] and the destabilizing effect of shear [represented in (9) by $\Delta\mathbf{u}$]. We are unaware of convincing theoretical support for this constraint. However, (11) has been shown to be approximately consistent with laboratory studies of mixing in stratified fluids (Price 1979) and to produce realistic results when applied to the oceanic surface mixed layer (e.g., Price et al. 1986).

The integrated equations describing the behavior of the boundary layer are (4), (5), (6) and (11). The required forcing function is $v_I(t)$, and the initial condition for motion beginning from rest is $B = 0$ at the initial time $t = 0$. The integrated momentum equations (4) and (5) describe the quasi-steady response of $\bar{u}$ and $\bar{v}$ to the instantaneous interior velocity $v_I(t)$, height $h(t)$ and buoyancy deficit $B(t)$. The buoyancy equation (6) describes the evolution of $B(t)$ due to cross-isobath advection, and the constraint (11) determines whether and how $h(t)$ increases. In this model, the height of the boundary layer cannot decrease.

Numerical solution of (4), (5), (6) and (11) is straightforward. In a time-stepping procedure, the solution at each new time step, given the solution at the previous time step, may be obtained as follows. First B is incremented according to (6), and then (4) and (5) are solved simultaneously for $\bar{u}$ and $\bar{v}$, with h held fixed at the value obtained during the previous time step. If R_b is, at this point, greater than or equal to unity, the solution advances to the next time step. If R_b is less than unity, (4), (5) and (11) are solved simultaneously for $\bar{u}$, $\bar{v}$ and h, with (11) as an equality, before advancing to the next time step. All of the numerical results presented in this paper are based on this time-stepping procedure.

The integrated model, as formulated above, reflects two basic assumptions. The first is that the boundary layer is well mixed, so that the density and velocity averaged over the thickness of the boundary layer are representative of the density and velocity everywhere within the boundary layer. The second is that the growth of the boundary layer is limited by a balance between the competing effects of stratification and shear, so that (11) is a realistic constraint on the height of the boundary layer.

3. Model results

a. *Comparison with Weatherly's and Martin's (1978) computations*

A comparison of numerical simulations reported by Weatherly and Martin (1978) with computations based on (4), (5), (6) and (11) is useful to help establish the validity of the integrated model. Weatherly's and Martin's simulations were based on the Mellor–Yamada (1974) level-two turbulence closure, in which turbulent transport of density and momentum are represented by gradient transport relationships, and the effective viscosity and diffusivity are products of a turbulent velocity scale, determined from an approximate turbulent energy balance, and an imposed turbulent length scale.

Weatherly and Martin (1978) presented three cases suitable for comparison with the integrated model. In the first case, the bottom was horizontal (i.e., $\alpha = 0$), and the second and third cases treated, respectively, upwelling-favorable (v_I negative) and downwelling-favorable (v_I positive) flows over sloping bottoms. In all cases, the interior along-isobath flow speed increased linearly from zero to 15 cm s^{-1} during the first 48 hours, and was then constant until the end of the computational period, which was 120 hours. The density was a function only of temperature. The interior buoyancy frequency N was 1.28×10^{-2} s^{-1}, the Coriolis parameter f was 0.63×10^{-4} s^{-1}, and the bottom slopes α were 2.4×10^{-3} and 2.6×10^{-4} in the upwelling and downwelling cases, respectively.

Our computations are based on the numerical time-stepping procedure described in the previous section. Since we are using an integrated model, the velocity and temperature fields are treated as if they were independent of z within the boundary layer, although this simplification is not necessarily implied by the model. In all cases a drag coefficient of 2.5×10^{-3} is used. According to Weatherly and Martin (1978), the

effective bottom roughness parameter z_o in their calculations was approximately 0.06 cm. A drag coefficient of 2.5×10^{-3} is appropriate for this roughness if one assumes an approximately logarithmic velocity profile within the boundary layer and a boundary layer height on the order of 5 to 10 m (e.g., Shlichting 1979). The computations of Weatherly and Martin (1978) indicate approximately logarithmic velocity profiles, and the boundary layer heights are on the order of 5 to 10 m (see Figs. 3 through 6, discussed below).

Figure 3 shows results for the case of a horizontal bottom. In this case, B remains fixed at its initial value of zero, and the integrated governing equations, which reduce to (4), (5) and (11), contain no temporal derivatives, so that they describe a boundary layer that adjusts immediately to the instantaneous interior velocity. Weatherly's and Martin's (1978) computations indicate fairly uniform velocity and temperature profiles within the boundary layer, although there is strong shear in the velocity profile near the bottom.

Figures 4, 5 and 6 show results for the upwelling and downwelling cases. Figure 4, which shows bottom temperature as a function of time, illustrates the cooling trend that results from upslope Ekman transport of cold water during upwelling, as well as the opposite warming trend that occurs during downwelling. Figure 5a, which shows temperature profiles at different stages during upwelling, shows that the boundary layer thickens initially and then reaches a fixed height of approximately 5 m, which is substantially smaller than the height reached in the case of a horizontal bottom (Fig. 3). In contrast, Fig. 5b shows temperature profiles during downwelling, which indicate more rapid growth of the boundary layer than during upwelling, and no tendency to reach a fixed height. Figures 5a and 5b also show that temperature gradients near the top of the boundary layer are much larger during upwelling than they are during downwelling. Figure 6 shows temperature and velocity profiles for the upwelling case at t equal to 4 days. Weatherly's and Martin's (1978) computations in Fig. 6 indicate more vertical structure in flow direction than is apparent in the case of a horizontal bottom (Fig. 3).

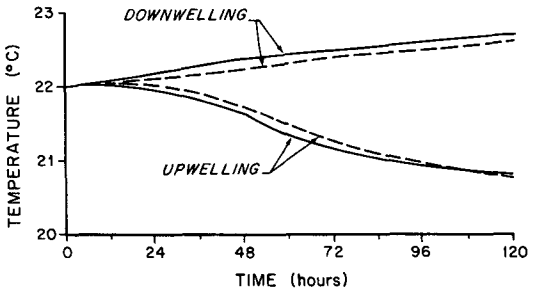

FIG. 4. Bottom temperature as a function of time for the upwelling ($\alpha = 2.4 \times 10^{-3}$) and downwelling ($\alpha = 0.26 \times 10^{-3}$) cases treated by Weatherly and Martin (1978). The solid lines are our computations and the dashed lines are the Weatherly and Martin computations.

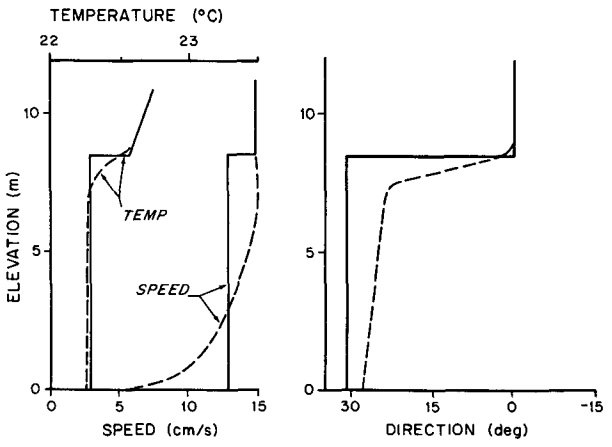

FIG. 3. Velocity and temperature for the case treated by Weatherly and Martin (1978) for stably stratified flow above a horizontal bottom ($\alpha = 0$). The solid lines are our computations and the dashed lines are the Weatherly and Martin computations.

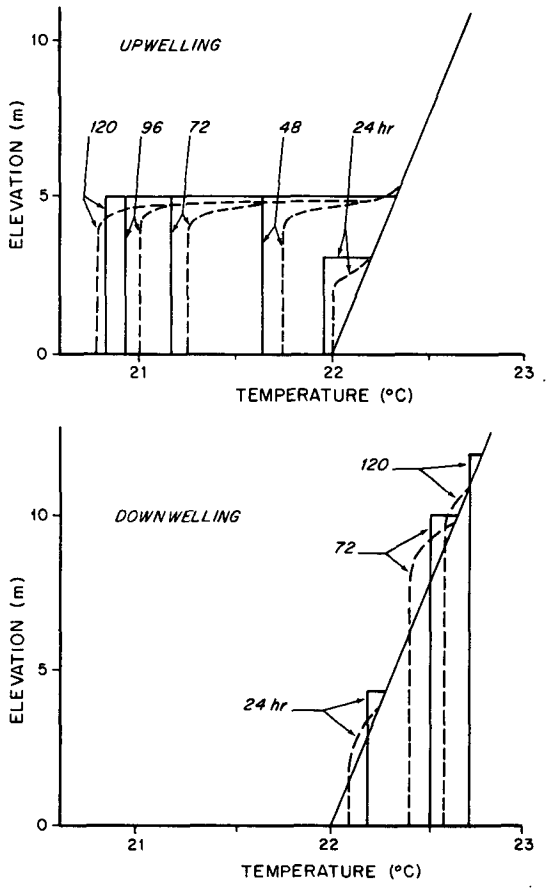

FIG. 5. Temperature profiles at different times for the upwelling problem (a) and for the downwelling problem (b) treated by Weatherly and Martin (1978). The solid lines are our computations and the dashed lines are the Weatherly and Martin computations.

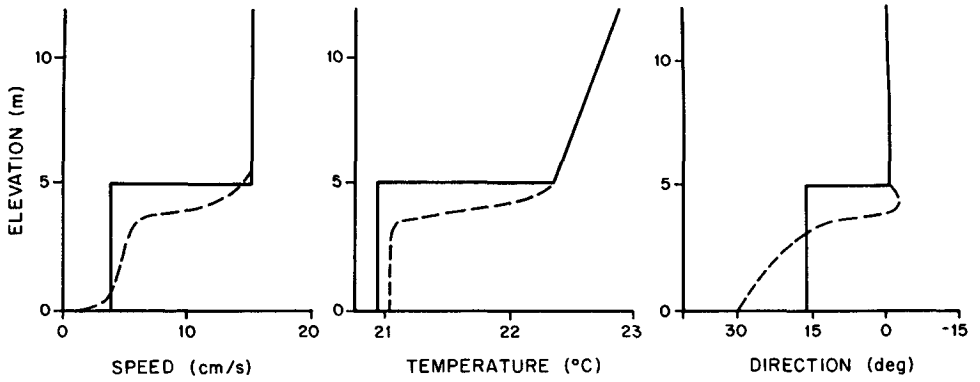

FIG. 6. Temperature, speed and direction profiles for the upwelling case treated by Weatherly and Martin (1978) at t equal to 4 days. The solid lines are our computations and the dashed lines the Weatherly and Martin computations. [Note: we are puzzled by differences between their temperature computations in Figs. 5a and 6 (Figs. 9c and 10 in their paper), which should be the same at 96 hours. In particular, there seems to be a difference in the height of the boundary layer. It is possible that some of these results were misplotted in the Weatherly and Martin paper. This possibility does not affect our qualitative conclusions.]

Although Weatherly's and Martin's (1978) computations show vertical structure that cannot be captured by an integrated model, Figs. 3 through 6 indicate overall good agreement, in terms of the bulk properties of the boundary layer, between the predictions of the integrated model and the more detailed turbulence closure computations. The favorable agreement is encouraging because we have made no attempt to tune the integrated model by varying the drag coefficient or the critical value of the bulk Richardson number.

b. *Response to impulsively applied forcing*

To determine the physics and parameter dependence described by the integrated model under conditions beyond those treated by Weatherly and Martin (1978), it is convenient to consider forcing in which $v_I(t)$ is zero for t less than zero, and equal to a nonzero constant for t greater than or equal to zero. Under this impulsively applied forcing, the solution indicates instantaneous mixing to a finite height at $t = 0$, followed by evolution toward a steady state as t approaches infinity. The results of the analysis may conveniently be expressed in terms of the dimensionless parameters β and γ, defined by

$$\beta = \frac{\sqrt{2}}{2}\frac{C_d N}{f}, \tag{12}$$

$$\gamma = \sqrt{2}\frac{\alpha N}{f}. \tag{13}$$

For fixed N/f, β may be regarded as a measure of the strength of bottom friction, and γ may be regarded as a measure of the influence of bottom slope. The quantities β and γ appear as the only parameters if one expresses the problem in dimensionless form by normalizing t by f^{-1}, $\bar{u}$ and $\bar{v}$ by $|v_I|$, h by $|v_I|N^{-1}$, and B by $|v_I|^2$. We first present the initial and steady-state solutions, and then discuss the characteristics of the transient evolution. As before, we refer to the case of negative v_I (positive $\bar{u}$) as upwelling, and to the case of positive v_I (negative $\bar{u}$) as downwelling.

The initial solution at $t = 0$, just after v_I jumps from zero to a finite value, corresponds to $B = 0$, because B becomes nonzero due to cross-isobath advection only after a finite time. The mixing criterion (11) is assumed to be marginally satisfied during the initial mixing process, so that (11) must be an equality in the initial solution. The solution to (4) and (5) with B equal to zero and (11) an equality is identical to the solution for a horizontal bottom, and was found in that context by Thompson (1973) to be

$$\bar{u} = -\frac{\sqrt{\beta}v_I}{1+\beta}, \tag{14}$$

$$\bar{v} = \frac{v_I}{1+\beta}, \tag{15}$$

$$h = 2^{1/4}\frac{u_*}{\sqrt{fN}} = \left(\frac{2\beta}{1+\beta}\right)^{1/2}\frac{|v_I|}{N}. \tag{16}$$

Here u_* is the shear velocity, defined by $u_* = \sqrt{\tau_b/\rho_o}$, where τ_b is the magnitude of the bottom shear stress. The initial solution for h is consistent with the scaling introduced by Zilitinkevich (1972) and with the large-stratification limit of the empirical expression (based on numerical simulations) proposed by Weatherly and Martin (1978), in which the height of the stably stratified mixed layer over a horizontal bottom is proportional to $u_*/\sqrt{fN}$.

The steady-state solution may be found by setting dB/dt equal to zero in the buoyancy equation (6). It follows from (6) and the along-isobath momentum

equation (5) that, in a steady-state solution with nonzero h,

$$\bar{u} = \bar{v} = 0 \tag{17}$$

so that the velocity averaged over the thickness of the boundary layer is zero. The cross-isobath momentum equation (4) reduces to

$$-fhv_I = \alpha B. \tag{18}$$

Substitution of (17) and (18) into (11) yields a quadratic equation for h. The solution satisfying the constraint that h must be non-negative is

$$h \geq \frac{\sqrt{2}}{\gamma}(\sqrt{1+\gamma^2} \pm 1)\frac{|v_I|}{N} \tag{19}$$

where the plus sign corresponds to downwelling ($v_I > 0$) and the minus sign corresponds to upwelling ($v_I < 0$). Inequality (19) shows that the minimum steady-state height for downwelling is always greater than the minimum steady-state height for upwelling. Although the steady-state solution is an exact solution to the integrated model equations and is important in understanding the transient behavior of the boundary layer, we believe that it does not represent a state that a real boundary layer could achieve, for reasons discussed in section 4b.

Computations indicate that the boundary layer evolves from the initial solution given by (14) through (16) toward the steady-state solution given by (17) through (19) as t increases from zero toward positive infinity. Analysis of the transient evolution between the initial and steady states is complicated algebraically, and the details of the analysis are given in the Appendix. Here we simply present the results, focusing on the initial transient evolution, because the solution is believed to become unrealistic as it approaches a steady state. In the upwelling case (v_I negative), the height h either remains fixed at its initial value for all t or remains fixed for a while before beginning to increase toward its minimum steady-state value, depending on whether γ is smaller or larger than a critical value γ_c, defined by

$$\gamma_c = 2\sqrt{\beta(1+\beta)}. \tag{20}$$

In the downwelling case (v_I positive), the height h always increases from its initial value toward its minimum steady-state value, and either begins to increase immediately at $t = 0$ or remains fixed for a while before beginning to increase, depending on whether γ is smaller or larger than a critical value γ_c, defined by

$$\gamma_c = (1+2\beta)\left(\frac{1+\beta}{\beta}\right)^{1/2}. \tag{21}$$

In cases for which dh/dt is initially zero, the velocity within the boundary layer begins immediately to decay toward its steady-state value of zero, and a time scale for the initial evolution may be obtained from the following expression for the initial rate of change of the along-isobath velocity:

$$\frac{1}{\bar{v}}\frac{d\bar{v}}{dt} = -\frac{\sqrt{\beta}\gamma^2 f}{2(1+\beta)(1+2\beta)} \quad \text{when} \quad t = 0. \tag{22}$$

In cases for which dh/dt is initially nonzero, the velocity within the boundary layer may either increase or decrease initially, and a time scale for the initial evolution may be obtained from the following expression for the initial rate of change of h:

$$\frac{1}{h}\frac{dh}{dt} = \frac{\gamma}{4}\frac{1+2\beta}{(1+\beta)^{3/2}}\left[1 - \frac{\gamma}{1+2\beta}\left(\frac{\beta}{1+\beta}\right)^{1/2}\right]f \quad \text{when} \quad t = 0. \tag{23}$$

It is a general feature of these results that the boundary layer is thicker during downwelling-favorable flows than it is during equally strong upwelling-favorable flows.

To illustrate the above results, conditions treated in Weatherly's and Martin's (1978) calculations for upwelling are first considered, in which $f = 0.63 \times 10^{-4}$ s^{-1}, $\alpha = 2.4 \times 10^{-3}$, $N = 1.28 \times 10^{-2}$ s^{-1} and $|v_I| = 15$ cm s^{-1}. As before, $C_d = 2.5 \times 10^{-3}$ is used. The corresponding values of the frictional parameter β and the slope parameter γ are approximately 0.36 and 0.69, respectively. Under these conditions, the initial solution is identical to the solution illustrated in Fig. 3. In the initial solution, the boundary layer thickness is approximately 8 m, the flow speed in the boundary layer is approximately 85% of the interior flow speed, and the Ekman veering within the boundary layer is approximately 30°. The minimum steady-state height for upwelling is approximately 5 m, which is smaller than the initial height, and the minimum steady-state height for downwelling is approximately 50 m, which is almost an order of magnitude larger than the initial height.

With β equal to 0.36 and γ equal to 0.69, γ is smaller than the critical values γ_c defined by both (20) and (21), so that we expect h to remain fixed at its initial value for all times during upwelling and to begin increasing immediately toward its minimum steady-state value during downwelling. In the upwelling case, the time scale for the initial evolution of $\bar{v}$, obtained from (22) is approximately $16f^{-1}$, or approximately 70 hours if $f = 0.63 \times 10^{-4}$ s^{-1}. The time scale for initial evolution of h during downwelling, determined from (23), is approximately $7f^{-1}$, or approximately 30 hours if $f = 0.63 \times 10^{-4}$ s^{-1}. Figures 7 and 8 show dimensionless height and velocity as functions of dimensionless time for the upwelling and downwelling cases, respectively. As expected, h remains constant for all times in the upwelling case, and h begins to increase immediately toward the minimum steady-state value in the downwelling case. The evolution is consistent with the estimates of the initial time scales. The evolution of the velocity within the boundary layer toward

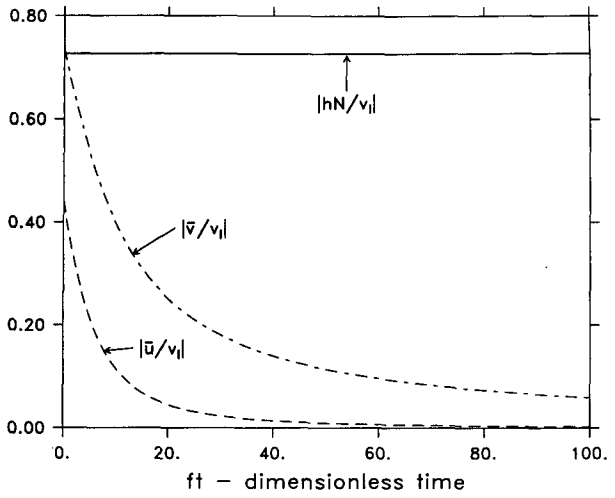

FIG. 7. Numerical computations based on the integrated model, for upwelling-favorable steady forcing applied impulsively at $t = 0$, with $\beta = 0.36$ and $\gamma = 0.69$. In this case $\bar{v}$ and v_l are negative and $\bar{u}$ is positive.

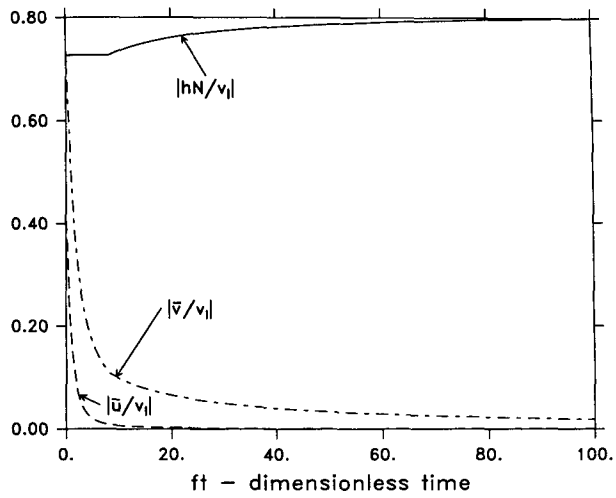

FIG. 9. Numerical computations based on the integrated model, for upwelling-favorable steady forcing applied impulsively at $t = 0$, with $\beta = 0.36$ and $\gamma = 1.73$. In this case $\bar{v}$ and v_l are negative and $\bar{u}$ is positive.

zero is slower in the downwelling case than it is in the upwelling case.

To illustrate the other type of qualitative behavior possible during upwelling, we consider $\beta = 0.36$ and $\gamma = 1.73$, which corresponds to a bottom slope 2.5 times greater than in the first example, for fixed C_d, N and f. In this case γ is larger than the critical value γ_c defined by (20), so that h is expected to remain constant for a while and then begin increasing during upwelling. Figure 9 confirms this expectation. It is interesting to note that the initial evolution of $\bar{u}$ and $\bar{v}$, during the period in which h is constant, is much more rapid than the later evolution, during the period in which h evolves.

To illustrate the other type of qualitative behavior possible during downwelling, we consider $\beta = 0.36$ and $\gamma = 13.8$, which corresponds to a bottom slope 20 times greater than in the first example, for fixed C_d, N and f. In this case γ is larger than the critical value γ_c defined by (21), so that h is expected to remain constant for a while and then begin increasing. Figure 10 shows that this expectation is correct. The period of initial evolution, in which h is fixed, is very short, and the initial evolution of $\bar{u}$ and $\bar{v}$ is very rapid.

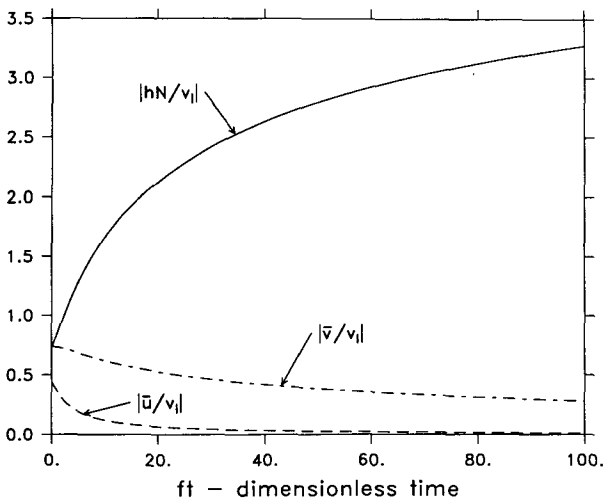

FIG. 8. Numerical computations based on the integrated model, for downwelling-favorable steady forcing applied impulsively at $t = 0$, with $\beta = 0.36$ and $\gamma = 0.69$. In this case $\bar{v}$ and v_l are positive and $\bar{u}$ is negative.

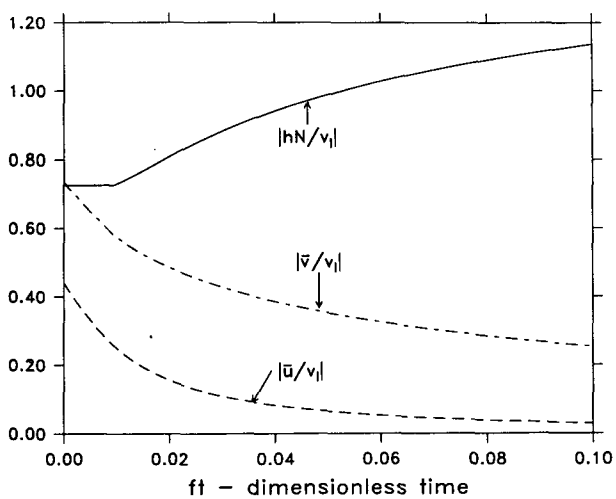

FIG. 10. Numerical computations based on the integrated model, for downwelling-favorable steady forcing applied impulsively at $t = 0$, with $\beta = 0.36$ and $\gamma = 13.8$. In this case $\bar{v}$ and v_l are positive and $\bar{u}$ is negative.

Lentz and Trowbridge (1991) give a comparison of model results and CODE observations, and they address the question of the applicability of a one-dimensional model to the CODE region. Here, a few computations are presented to illustrate the relevance of the model to the observations shown in Fig. 1. Conditions typical of the CODE region are $f = 10^{-4}$ s^{-1}, $\alpha = 5 \times 10^{-3}$ and $N = 10^{-2}$ s^{-1}. A reasonable value of C_d for conditions without significant surface waves is 2.5×10^{-3}, based on an approximately logarithmic velocity profile in a boundary layer of thickness 10 m above a bottom with a roughness parameter z_o of 0.1 cm, corresponding to relief with a scale of 3 cm (see Grant et al. 1984). Under these conditions, β is approximately 0.18 and γ is approximately 0.71. This value of γ is smaller than the critical values γ_c defined by (20) and (21), so that, under impulsively applied forcing, the boundary layer maintains its initial height for all times during upwelling, and begins immediately to grow toward its minimum steady-state height during downwelling. These results are qualitatively consistent with observations, in which mixed layer heights for comparable flow speeds are greater during downwelling than they are during upwelling. For an interior velocity of 20 cm s^{-1} the initial height of the boundary layer is approximately 11 m, comparable to observed mixed layer heights during upwelling. The time scale for initial evolution of $\bar{v}$ during upwelling, calculated from (22), is approximately 42 hours. The time scale for initial evolution of h during downwelling, calculated from (23) is approximately 18 hours. These time scales are comparable to or shorter than the time scale of the forcing, so that one expects to observe significant departures from the initial solution.

4. Discussion

a. *Physics of the model behavior*

The key results based on the integrated model, for the transient problem in which motion begins from rest, are: 1) favorable comparison with Weatherly's and Martin's (1978) turbulence closure computations; 2) rapid mixing near the onset of forcing to a height proportional to $u_*/\sqrt{fN}$; 3) evolution in which h either remains fixed at its initial value or increases, depending on the direction of the forcing and on the values of the frictional parameter β and the slope parameter γ; 4) asymptotic approach to a steady state in which the vertically averaged velocity within the boundary layer is zero; and 5) thicker mixed layers during downwelling-favorable flows than during comparably strong upwelling-favorable flows.

The favorable comparison between the integrated model results and the turbulence closure computations provides support for the applicability of the integrated model, at least under the conditions treated by Weatherly and Martin (1978). In addition, the favorable comparison indicates that the bulk characteristics of Weatherly's and Martin's simulations may be understood simply as consequences of integral momentum and buoyancy conservation, coupled with mixing processes that maintain the bulk Richardson number at values grater than approximately unity. In this sense, Weatherly's and Martin's simulations are consistent with results of stress-driven laboratory entrainment experiments (Price 1979) and with the behavior of the oceanic surface mixed layer (Price et al. 1986).

In the solution $h \propto u_*/\sqrt{fN}$ for the initial height of the boundary layer, both interior stratification and planetary rotation limit the height to which the layer can extend. This expression contrasts with the classical result for the unstratified case, in which the height of the boundary layer is limited only by planetary rotation, and $h \propto u_*/f$ (e.g., Blackadar and Tennekes 1968). One constraint on the validity of the present analysis is that the ratio of the initial height $u_*/\sqrt{fN}$ to the unstratified scale height u_*/f be less than order unity, in order to justify the basic assumption that stratification plays a key role in limiting the height of vertical mixing.

The small-time evolution of the height h, as described by the integrated model, is the product of two competing effects. The first is cross-isobath advection of buoyancy, which increases the bulk Richardson number in the upwelling case, therefore retarding vertical mixing, while reducing the bulk Richardson number in the downwelling case, therefore enhancing vertical mixing. The second effect is the evolution of the velocity within the boundary layer, which may either promote or retard vertical mixing by increasing or reducing the velocity jump across the top of the boundary layer, depending on the precise circumstances. If the slope parameter γ is sufficiently small [i.e., if γ is smaller than the critical values defined by (20) and (21)], then cross-isobath advection of buoyancy is the dominant effect, so that the boundary layer height stays fixed as a result of a stabilizing buoyancy flux during upwelling (Fig. 7), and begins to grow immediately as a result of a destabilizing buoyancy flux during downwelling (Fig. 8). If γ is larger [i.e., if γ is larger than the critical values defined by (20) and (21)], then the evolution of the shear across the top of the boundary layer becomes the dominant effect, so that different types of behavior occur (Figs. 9 and 10).

The asymptotic approach to a steady state may be understood by examining the qualitative structure of the density field (Fig. 11). We consider first the upwelling case, which corresponds to forcing by a dynamic pressure gradient that tends, in the absence of rotation, to push water upslope. Just after the initial mixing process, the integrated density anomaly $\int_0^{+\infty} (\rho - \rho_I) dz$ is zero (Fig. 11a). After a finite time interval, the boundary layer is denser than it was initially, as a result of cross-isobath advection (Fig. 11b). The integrated buoyancy force on the boundary layer

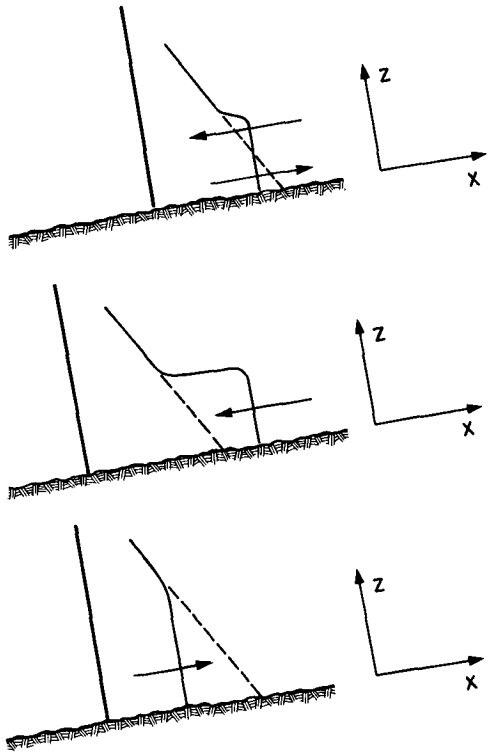

FIG. 11. (a) Density profile at $t = 0$ just after impulsive application of steady forcing, showing existence of a boundary layer. The dashed line is the initial density profile. (b) Density field for $t > 0$ during upwelling, showing existence of a large density excess in the boundary layer. (c) Density field for $t > 0$ during downwelling, showing existence of a density deficit in the boundary layer. In (a) the arrows indicate the sense of the z-dependent buoyancy force associated with the density anomaly in the boundary layer. In (b) and (c) the arrows indicate the sense of the integrated buoyancy force acting on the boundary layer.

due to the density anomaly is downslope, in opposition to the forcing by the dynamic pressure gradient. Thus the magnitude of the net force on the boundary layer is smaller than it was initially, and consequently the velocity within the boundary layer must also be smaller than it was initially. As time passes and the upwelling process continues, the buoyancy force more nearly balances the constant forcing by the dynamic pressure gradient, so that the velocity within the boundary layer continues to evolve toward zero. During downwelling the process is the same except that in this case the dynamic pressure gradient is downslope and the gravitational force is upslope (Fig. 11c).

In the model, thicker boundary layers occur during downwelling-favorable flows than during comparably strong upwelling-favorable flows because of cross-isobath advection of buoyancy, which tends to reduce the bulk Richardson number during downwelling and increase it during upwelling. This model result is qualitatively consistent with estimates of bottom mixed-layer height obtained from CODE observations, as is discussed in more detail by Lentz and Trowbridge (1991).

b. *Breakdown of the integrated model at large times*

Although the steady-state solution given by (17) through (19) is an exact solution to the integrated model equations and is important in understanding the transient behavior of the boundary layer, it does not, in our opinion, represent a configuration that a real boundary layer could reach. The reason is that the integrated model is a plausible approximation only if the velocity within the boundary layer is fairly uniform, as stated in section 2. In contrast, if a real boundary layer were to reach a state in which the integral cross-isobath momentum balance is (18), it would have a nonuniform velocity profile, probably including a reversal in flow direction, as a result of a nonuniform buoyancy force acting on the boundary layer.

To demonstrate a nonuniform buoyancy force under conditions in which the vertically integrated cross-isobath momentum balance is (18), we write the cross-isobath momentum equation (1) as follows, assuming that the density ρ is nearly independent of z within the well-mixed boundary layer:

$$-fv + \frac{\partial}{\partial z}\langle u'w'\rangle \approx -\left(fv_I + \frac{\alpha B}{h}\right) - \alpha N^2\left(z - \frac{1}{2}h\right). \quad (24)$$

The first term on the right side of (24) is the vertically uniform component of the force acting on the boundary layer. The last term in (24) is a nonuniform force resulting from the nonuniform distribution of ρ_I in (1). The uniform component of the forcing is represented in the integrated model. The nonuniform component of the forcing is not represented explicitly in the integrated model, and must be balanced in a real flow. If (18) were satisfied, then the uniform component of the forcing would be zero, and (24) would reduce to

$$-fv + \frac{\partial}{\partial z}\langle u'w'\rangle \approx -\alpha N^2\left(z - \frac{1}{2}h\right). \quad (25)$$

The vertically nonuniform force on the right side of (25) is upslope (positive) in the lower half of the boundary layer and downslope (negative) in the upper half of the boundary layer.

If a boundary layer were to reach a state with a vertically integrated cross-isobath momentum balance given by (18), then the velocity within the boundary layer would be determined by the approximate cross-isobath momentum equation (25) and by the along-isobath momentum equation (2). The precise structure of the velocity field described by these equations cannot be determined in the absence of constitutive equations. The qualitative features of two limiting cases are straightforward, however. In the limit in which the Coriolis term on the left side of (25) is vanishingly small

in comparison to the stress term, (25) suggests a cross-isobath flow that is upslope in the lower half of the boundary layer and downslope in the upper half of the boundary layer. In the opposite limit, in which the stress term on the left side of (25) is vanishingly small in comparison to the Coriolis term, (25) describes a uniformly sheared along-isobath flow, which is positive in the upper half of the boundary layer and negative in the lower half of the boundary layer. In intermediate cases in which the Coriolis and stress terms in (25) are comparable to each other, the flow described by (25) and (2) is more complex than in either limiting case, but probably contains a reversal in direction, as a result of the reversal in the direction of the forcing.

The vertically nonuniform, reversing flow structure suggested by (25) is inconsistent with the assumption of a fairly uniform velocity profile that is basic to the integrated model, especially if the vertically averaged velocity is zero, as indicated by the steady-state expressions (17). In particular, use of a quadratic drag law relating bottom stress to vertically averaged velocity is not reasonable, because the vertically averaged velocity is not representative of the velocity near the bottom, where the bottom stress is transmitted to the water column. Similarly, use of a mixing criterion relating growth of the boundary layer to vertically averaged velocity is not reasonable, because the vertically averaged velocity is not representative of the velocity near the top of the boundary layer, where the vertical mixing occurs that causes the growth of the layer. We therefore conclude that the integrated model breaks down before it reaches a steady state, and that the steady-state configuration described by the integrated model is unlikely to be realistic.

An appreciation for the breakdown of the integrated model at large times may be obtained by examining the behavior of the quantity μ, defined by

$$\mu = \frac{\frac{1}{2}\alpha N^2 h}{|fv_I + \alpha B/h|}. \tag{26}$$

This quantity is a measure of the strength of the nonuniform component of the forcing relative to the uniform component of the forcing in (24). This quantity is probably not the only parameter controlling the breakdown of the integrated model. However, if μ is substantially larger than unity, the above discussion suggests that the flow within the boundary layer is nonuniform and that the integrated model is not realistic.

Figure 12 shows μ as a function of dimensionless time ft under impulsively applied forcing for three cases. The first is the upwelling case treated by Weatherly and Martin (1978) and shown in Fig. 7, in which $\alpha = 2.4 \times 10^{-3}$. The second is the downwelling case, shown in Fig. 8, in which $\alpha = 2.4 \times 10^{-3}$. The third is the downwelling case treated by Weatherly and Martin, in which $\alpha = 2.6 \times 10^{-4}$. In all three cases, $f = 0.63 \times 10^{-4}$ s^{-1}, $N = 1.28 \times 10^{-2}$ s^{-1}, $C_d = 2.5 \times 10^{-3}$, and $|v_I| = 15$ cm s^{-1}. In the upwelling and downwelling cases with relatively steep slopes ($\alpha = 2.4 \times 10^{-3}$), μ exceeds order unity after ft exceeds approximately 30, suggesting that the integrated model breaks down at ft substantially larger than 30. In the downwelling case with a relatively mild slope ($\alpha = 2.6 \times 10^{-4}$), μ remains very small throughout the whole of the computational period, because of the small value of γ and the correspondingly long evolution time [see (23)]. The dimensionless time in the Weatherly and Martin computations was limited to values smaller than approximately 30, and at these relatively small times μ is of order unity or smaller in both of the sloping-bottom cases that they examined (cases 1 and 3 in Fig. 12). Figure 12 suggests that if Weatherly and Martin had carried out computations for substantially larger times in their upwelling case, they would have encountered behavior that would not have been reproduced well by the integrated model.

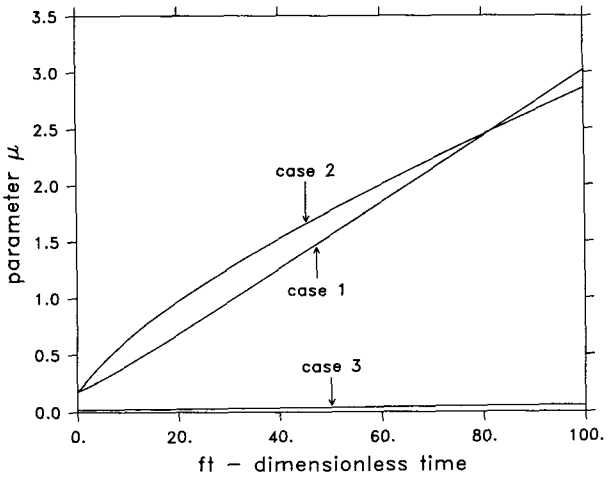

FIG. 12. The quantity μ [defined in (26)] as a function of dimensionless time ft, from computations based on the integrated model under impulsively applied forcing. In all three cases, $f = 0.63 \times 10^{-4}$ s^{-1}, $N = 1.28 \times 10^{-2}$ s^{-1}, $C_d = 2.5 \times 10^{-3}$, and $|v_I| = 15$ cm s^{-1}. Cases 1 and 2 are upwelling and downwelling cases, respectively, with $\alpha = 2.4 \times 10^{-3}$. Case 3 is a downwelling case with $\alpha = 2.6 \times 10^{-4}$.

c. *Behavior of the boundary layer at large times*

The discussion in the previous subsection indicates that the integrated model breaks down at sufficiently large times, as a result of increasingly important nonuniform buoyancy forces acting on the boundary layer. We present here some simple ideas about the structure and evolution of the boundary layer at large times, after the integrated model has become unrealistic. We concentrate on the downwelling case, for which some qualitative observational evidence is available.

The present discussion is based on two assumptions. The first is that the downwelling process, as a result of the tendency to advect light water beneath dense water, produces at large times a density structure that varies continuously from a well-mixed profile within the

boundary layer to a stably stratified profile in the interior, without abrupt changes in density near the top of the boundary layer. The buoyancy anomaly within the boundary layer may then be written

$$\frac{g}{\rho_o}(\rho - \rho_I) \approx N^2(z - h). \tag{27}$$

The second assumption is that the stress term in the cross-isobath momentum equation (1) is small in comparison to the Coriolis term, during late stages of downwelling, so that (1) reduces approximately to

$$-fv \approx -fv_I - \frac{\alpha g}{\rho_o}(\rho - \rho_I). \tag{28}$$

Substitution of (28) into (27) yields the following expression for the along-isobath velocity within the boundary layer:

$$v \approx v_I + \frac{\alpha N^2}{f}(z - h). \tag{29}$$

Equation (29) describes a velocity profile that varies linearly from the interior velocity v_I at $z = h$ to a bottom velocity v_b at $z = 0$, where v_b is given by

$$v_b = v_I - \frac{\alpha N^2 h}{f}. \tag{30}$$

Equation (29) cannot be valid within the constant stress layer near the bottom, where the velocity presumably varies logarithmically. Equation (29) is a plausible approximation elsewhere in the boundary layer, however.

Integration of (2) over the thickness of the boundary layer shows that the cross-isobath Ekman flux is proportional to the y component of the bottom stress and that a downwelling Ekman flux corresponds to a bottom stress with a positive y component. A bottom stress with a positive y component presumably corresponds to positive v_b. The present analysis of the late stages of downwelling therefore requires positive v_b.

Figure 13 shows the qualitative structure of the density and velocity profiles described by (27) and (29). As t increases and the downwelling process continues, the height of the boundary layer grows in response to the continuous downslope advection of light water within the boundary layer. As h increases, the bottom velocity v_b decreases, according to (30), and the y component of the bottom stress and the cross-isobath Ekman flux presumably also decrease. These ideas indicate approach to a state in which the bottom velocity, along-isobath bottom stress and Ekman flux are zero, so that further evolution of the boundary layer ceases. In this steady-state limit the height of the boundary layer, determined by setting v_b equal to zero in (30), is

$$h = \frac{fv_I}{\alpha N^2} = \frac{\sqrt{2}}{\gamma}\frac{v_I}{N}. \tag{31}$$

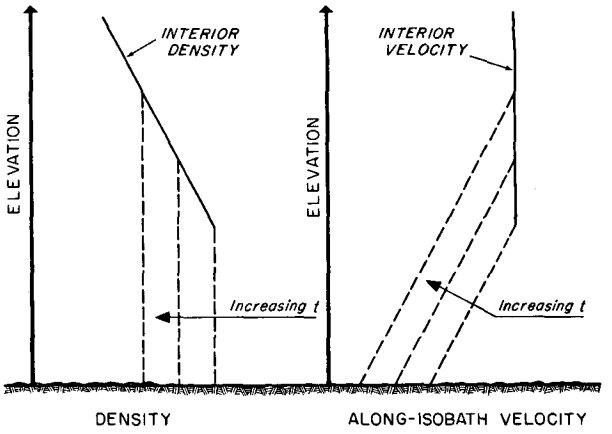

FIG. 13. Qualitative density and velocity fields in the bottom boundary layer at large times under downwelling-favorable forcing.

This steady-state height is always smaller than the steady-state height (19) given by the integrated model for the downwelling case. It should be noted that integration of (2) and (3) over the thickness of the boundary layer shows that in a steady state the along-isobath bottom stress must be zero, independently of the details of the velocity profile.

CODE observations provide qualitative observational support for the steady-state relationship (31) between h and v_I (Lentz and Trowbridge 1991). In addition, observational support for the qualitative structure of the density field shown in Fig. 13 is given by numerous conductivity–temperature–depth (CTD) profiles obtained over the sloping shelves off of Oregon, Peru and California, which indicate a well-mixed boundary layer and a smooth transition to a stably stratified interior, without large density jumps near the top of the boundary layer, when the boundary layer is thick, as during late stages of downwelling (e.g., Holbrook and Halpern 1972; Huyer et al. 1978). The density structure in Fig. 13 is a plausible consequence of the tendency for advection of light water beneath dense water during downwelling, when the growth of the boundary layer is possibly controlled by incipient gravitational instability near the top of the layer.

The velocity structure shown in Fig. 13 is a plausible consequence of (1) when the density in the boundary layer is well-mixed vertically and the bottom stress is small, so that the stress term in (1) may be expected to be small in comparison to the Coriolis term. The above analysis of late stages of downwelling suggests a vanishing bottom stress at large times, so that the assumption of a small stress term in (1) is internally consistent in the analysis. Support for the velocity structure shown in Fig. 13 is also provided by observations. Differentiation of (28) or (29) gives

$$\frac{\partial v}{\partial z} \approx \frac{\alpha N^2}{f}. \tag{32}$$

This expression describes an along-isobath thermal wind shear maintained by a cross-isobath density gradient $\partial\rho/\partial x$ within the boundary layer. Some observational support for (32) is provided by CODE measurements showing positive along-isobath shears, with magnitudes comparable to that given by (32), during one event when the bottom mixed layer was thick (Lentz and Trowbridge 1991). Additional support for (32) is provided by recent measurements, with better resolution of the bottom mixed layer than the CODE observations, obtained over the continental shelf off northern California (personal communication, B. Butman, U.S. Geological Survey, Woods Hole, Massachusetts).

Although observations support the existence of the along-isobath shear given by (32) when the boundary layer is thick, it is not clear at present how this shear is maintained in a well-mixed density field without producing Reynolds stresses that contribute significantly to the cross-isobath momentum balance, thus invalidating (28). Our current hypothesis is that, during late stages of downwelling, the turbulence does not in fact mix the density completely uniformly in z throughout the boundary layer, but instead leaves a small, stable density gradient sufficiently strong to suppress vertical mixing without destroying it completely. This idea is supported by a CTD profile obtained in CODE during an event in which the bottom mixed layer was thick and the along-isobath velocity within the mixed layer had a shear consistent with (32) (Lentz and Trowbridge 1991). The CTD profile indicates a weak, stable density gradient sufficiently strong to maintain a gradient Richardson number of approximately ¼ within the bottom mixed layer, suggesting a state of marginal stability with weak turbulence.

In the presence of the shear given by (32), the density gradient required to maintain the gradient Richardson number at a value of ¼ is

$$-\frac{g}{\rho_o}\frac{\partial\rho}{\partial z} \approx \frac{1}{4}\left(\frac{\alpha N^2}{f}\right)^2 = \frac{\gamma^2}{8}N^2. \qquad (33)$$

As an example, with γ equal to 0.69, as in Weatherly's and Martin's (1978) upwelling case, the density gradient given by (33) is approximately 17 times smaller than the interior density gradient. This density field would appear well mixed in the bottom boundary layer in all except the most accurate and carefully examined density measurements. If γ is larger, the density gradient given by (33) may be comparable to the interior density gradient. In this case, the analysis must be modified to account for the effect of vertically nonuniform ρ in the thermal wind balance (32). Thus, the arguments in this section are valid only for sufficiently small γ.

5. Conclusions

We have presented an analysis of the stably stratified, rotating boundary layer above a sloping bottom, under idealized conditions in which the boundary layer mixes from rest into a uniformly stratified interior with horizontal isopycnal surfaces and a spatially uniform, along-isobath interior velocity. The purpose of the analysis was to examine the observed asymmetric response of the boundary layer, in which the characteristics of the layer depends on the direction, in addition to the magnitude, of the interior velocity. The analysis is based on an integrated model, in which the bottom stress is determined from a quadratic drag law, and the height of the boundary layer is determined from a mixing criterion involving the bulk Richardson number (Pollard et al. 1973).

Results based on the integrated model compare favorably with the turbulence closure computations reported by Weatherly and Martin (1978), suggesting that the bulk features of the Weatherly and Martin simulations may be understood as consequences of integral conservation of momentum and buoyancy, coupled with mixing processes that maintain the bulk Richardson number at values greater than approximately unity. Under rapidly applied forcing, the integrated model indicates mixing at the onset of forcing to a height limited by both planetary rotation and interior stratification, followed by evolution in which the height of the boundary layer may either increase or remain fixed near its initial value, depending on the behavior of the buoyancy within the boundary layer and the shear across the top of the boundary layer. The model predicts reduction of the velocity within the boundary layer with increasing time, in response to increasingly important buoyancy forces that oppose the forcing by the dynamic pressure gradient. The solution asymptotically approaches a steady state in which there is no vertically integrated force acting on the boundary layer, and the velocity averaged over the thickness of the boundary layer is zero. The model indicates thinner boundary layers during upwelling-favorable flows than during comparably strong downwelling-favorable flows, in qualitative agreement with observations. This asymmetric behavior is a result of cross-isobath advection of buoyancy, which tends to retard vertical mixing during upwelling and to enhance vertical mixing during downwelling.

The integrated model is believed to break down at sufficiently large times under constant forcing, as a result of a vertically nonuniform buoyancy field that dominates the forcing as the solution approaches a steady state, suggesting a nonuniform velocity profile inconsistent with model assumptions. Simplified arguments for the downwelling case at large times suggest a structure in which the density field varies continuously from a well-mixed profile within the boundary layer to a stably stratified profile in the interior, and the along-isobath velocity is uniformly sheared as a result of a thermal wind balance in the cross-isobath momentum equation.

Although limited in applicability because of its simplicity, the model presented in this paper captures in a plausible way the asymmetric behavior apparent in the observations in which the response of the boundary layer depends on the direction, as well as the magnitude, of the interior velocity. In the model, the asymmetric response is due to the combined effects of stratification, planetary rotation, and a sloping bottom. The model shows how these effects influence the height and evolution of the boundary layer. The insight provided by the analysis may be useful in understanding more complex oceanic boundary layer flows.

Acknowledgments. This study was funded by the Office of Naval Research under the Coastal Sciences Program and the Marine Geology and Geophysics Program (Grants N00014-89-J-1067 and N00014-89-J-1074).

APPENDIX

Initial Transient Response to Impulsively Applied Forcing

Our computations indicate that, as t increases, the solution for impulsively applied forcing based on the integrated model evolves from the initial state given by (14) through (16) toward the steady state given by (17) through (19). Some information about the evolution between these two states may be inferred simply by comparing the two expressions for the height h. For upwelling, it can be shown that the initial height given by (16) is greater than the minimum steady-state height given by (19) if

$$\gamma < 2\sqrt{\beta(1+\beta)}. \tag{34}$$

If (34) is satisfied, it is reasonable to expect (and numerical computations confirm) that during upwelling h remains constant at its initial value as the boundary layer evolves toward a steady state. If (34) is not satisfied, it is reasonable to expect (and numerical computations confirm) that during upwelling h increases from its initial value toward its minimum steady-state value as t approaches infinity. Similarly, for downwelling it can be shown that the minimum steady-state height given by (19) is always greater than the initial height given by (16). It is therefore reasonable to expect, and numerical computations confirm, that during downwelling h always increases from its initial value to its minimum steady-state value as t increases.

To proceed further in an analysis of the temporal evolution, it is convenient to rewrite the integrated equations describing the boundary layer in a different way. For fixed v_I, the momentum equations (4) and (5) give $\bar{u}$ and $\bar{v}$ as functions of B and h, with t as a parameter. We therefore have

$$\frac{d\bar{u}}{dt} = \frac{\partial \bar{u}}{\partial B}\frac{dB}{dt} + \frac{\partial \bar{u}}{\partial h}\frac{dh}{dt}, \tag{35}$$

$$\frac{d\bar{v}}{dt} = \frac{\partial \bar{v}}{\partial B}\frac{dB}{dt} + \frac{\partial \bar{v}}{\partial h}\frac{dh}{dt}. \tag{36}$$

Similarly, the time derivative of $R_b(t)$ may be written, by differentiating (10),

$$\frac{1}{R_b}\frac{dR_b}{dt} = \psi_B \frac{dB}{dt} + \psi_h \frac{dh}{dt}, \tag{37}$$

where

$$\psi_B = \left(B + \tfrac{1}{2}N^2h^2\right)^{-1}\left[1 - 2R_b\bar{u}\frac{\partial \bar{u}}{\partial B} - 2R_b(\bar{v} - v_I)\frac{\partial \bar{v}}{\partial B}\right], \tag{38}$$

$$\psi_h = \left(B + \tfrac{1}{2}N^2h^2\right)^{-1}\left[N^2h - 2R_b\bar{u}\frac{\partial \bar{u}}{\partial h} - 2R_b(\bar{v} - v_I)\frac{\partial \bar{v}}{\partial h}\right]. \tag{39}$$

The partial derivatives on the right sides of these equations may be determined from the momentum equations (4) and (5), and are found, after straightforward algebra, to be

$$\frac{B}{\bar{u}}\frac{\partial \bar{u}}{\partial B} = \sin^2(\phi)\frac{1 + 2\tan^2(\phi)}{2 + \tan^2(\phi)}\frac{\alpha B}{fh\bar{v}}, \tag{40}$$

$$\frac{B}{\bar{v}}\frac{\partial \bar{v}}{\partial B} = \sin^2(\phi)\frac{\tan^2(\phi)}{2 + \tan^2(\phi)}\frac{\alpha B}{fh\bar{v}}, \tag{41}$$

$$\frac{h}{\bar{u}}\frac{\partial \bar{u}}{\partial h} = \sin^2(\phi)\frac{1 + 2\tan^2(\phi)}{2 + \tan^2(\phi)}\frac{v_I - \bar{v}}{\bar{v}} - \sin^2(\phi), \tag{42}$$

$$\frac{h}{\bar{v}}\frac{\partial \bar{v}}{\partial h} = \sin^2(\phi)\frac{\tan^2(\phi)}{2 + \tan^2(\phi)}\frac{v_I - \bar{v}}{\bar{v}} + \cos^2(\phi), \tag{43}$$

where ϕ is the angle between the velocity vector and the positive x axis, defined by

$$\phi = \tan^{-1}\left(\frac{\bar{v}}{\bar{u}}\right). \tag{44}$$

Equations (6), (35), (36) and (37) are a set of coupled, nonlinear, first-order, ordinary differential equations, which, together with the constraint (11) on the bulk Richardson number, determine the evolution of $\bar{u}$, $\bar{v}$, B, R_b and h.

The quantities dR_b/dt and dh/dt behave in a special way. If at any instant R_b is greater than unity, then (11) is satisfied and no vertical mixing occurs, so that dh/dt is zero. If R_b is equal to unity and cross-isobath advection of buoyancy would by itself increase R_b [i.e., if the first term on the right side of (37) is positive] then no vertical mixing is required to satisfy (11), and dh/dt is again zero. Finally, if R_b is equal to unity and cross-isobath advection of buoyancy would by itself reduce R_b [i.e., if the first term on the right side of (37) is negative] then h must increase slightly to maintain R_b at the critical value of unity, and dh/dt takes on

the value required to make the right side of (37) equal to zero. With this behavior, R_b can never become less than unity.

Information about the initial behavior of the transient solution may be inferred from the initial behavior of R_b. In the initial solution [(14) through (16)] the mixing criterion (11) is marginally satisfied, so that R_b is equal to unity. Substitution of (14) through (16) into (37) through (43) yields, when t is equal to zero,

$$\frac{1}{2}N^2h^2\frac{dR_b}{dt} = \left[1 - \frac{\gamma}{1+2\beta}\left(\frac{\beta}{1+\beta}\right)^{1/2}\frac{|v_I|}{v_I}\right] \times \frac{dB}{dt} + \frac{4\beta}{1+2\beta}\frac{v_I^2}{h}\frac{dh}{dt}. \quad (45)$$

The first term on the right side of (45) represents changes in R_b due to cross-isobath advection of buoyancy, and the second term represents changes in R_b due to changes in h. In the case of upwelling, it can easily be shown that the first term on the right side of (45) is always positive. During upwelling, then, cross-isobath advection of buoyancy initially increases R_b, so that vertical mixing does not occur and dh/dt is in all cases initially zero. In the case of downwelling, on the other hand, the first term on the right side of (45) is negative if

$$\gamma < (1+2\beta)\left(\frac{1+\beta}{\beta}\right)^{1/2}. \quad (46)$$

If (46) is satisfied, cross-isobath advection of buoyancy would, in the absence of other effects, decrease R_b at small times during downwelling. In this case h must begin to increase immediately in order to satisfy (11), and it does so in such a way that R_b maintains a constant value of unity. If (46) is not satisfied, h initially remains constant during downwelling.

For cases in which dh/dt is nonzero initially, we can determine the initial value of dh/dt by setting the left side of (45) equal to zero and substituting (6), (14) and (15). The result is

$$\frac{1}{h}\frac{dh}{dt} = \frac{\gamma}{4}\frac{1+2\beta}{(1+\beta)^{3/2}}\left[1 - \frac{\gamma}{1+2\beta}\left(\frac{\beta}{1+\beta}\right)^{1/2}\right]f \quad \text{when} \quad t = 0. \quad (47)$$

Similarly, an expression for the initial value of $d\bar{v}/dt$ can be obtained by substituting the initial solution into (6), (36), (41) and (43). The result is

$$\frac{1}{\bar{v}}\frac{d\bar{v}}{dt} = -\frac{\sqrt{\beta}\gamma^2 f}{2(1+\beta)(1+2\beta)} + \frac{2\beta}{1+2\beta}\frac{1}{h}\frac{dh}{dt} \quad \text{when} \quad t = 0. \quad (48)$$

Equations (47) and (48) give information about the initial behavior of the boundary layer, and may be used to obtain estimates of the inverses of the time scales for initial evolution of h and $\bar{v}$. Similar expressions can, of course, be obtained for $\bar{u}$ and any other quantity of interest.

REFERENCES

Abramowitz, M., and I. A. Stegun, eds., 1970: *Handbook of Mathematical Functions.* U.S. Govt. Printing Office,

Bird, A. A., G. L. Weatherly and M. Wimbush, 1982: A study of the bottom boundary layer over the eastward scarp of the Bermuda Rise. *J. Geophys. Res.*, **87**, 7941–7954.

Blackadar, A. K., and H. Tennekes, 1968: Asymptotic similarity in neutral barotropic planetary boundary layers. *J. Atmos. Sci.*, **25**, 1015–1020.

Eittreim, S., P. E. Biscaye and A. F. Amos, 1975: Benthic nepheloid layers and the Ekman thermal pump. *J. Geophys. Res.*, **80**, 5061–5067.

Garrett, C., 1990: The role of secondary circulation in boundary mixing. *J. Geophys. Res.*, **95**, 3181–3188.

Grant, W. D., A. J. Williams and S. M. Glenn, 1984: Bottom stress estimates and their prediction on the northern California continental shelf during CODE-1: The importance of wave-current interaction. *J. Phys. Oceanogr.*, **14**, 506–527.

Holbrook, J. R., and D. Halpern, 1972: STD measurements off the Oregon coast, July–August 1972. Coastal Upwelling Ecosystems Analysis Data Report 4. 381 pp.

Huyer, A., W. E. Gilbert, R. Schramm and D. Barton, 1978: CTD observations off the coast of Peru, R/V *Melville,* 4 March–22 May 1977, and R/V *Columbus Iselin,* 5 April–19 May 1977. Coastal Upwelling Ecosystems Analysis Data Report 55, Oregon State University, 409 pp.

Lentz, S. J., and J. H. Trowbridge, 1991: The bottom boundary layer over the northern California shelf. *J. Phys. Oceanogr.*, **21**, 1186–1201.

MacCready, P., and P. B. Rhines, 1991: Buoyant inhibition of Ekman transport on a slope and its effect on stratified spin-up. *J. Fluid Mech.*, **223**, 631–661.

Mellor, G. L., and T. Yamada, 1974: A hierarchy of turbulence closure models for planetary boundary layers. *J. Atmos. Sci.*, **31**, 1791–1806.

Phillips, O. M., 1977: *The Dynamics of the Upper Ocean.* Cambridge University Press.

Pollard, R. T., P. B. Rhines and R. O. R. Y. Thompson, 1973: The deepening of the wind-mixed layer. *Geophys. Fluid Dyn.*, **3**, 381–404.

Price, J. F., 1979: On the scaling of stress-driven entrainment experiments. *J. Fluid Mech.*, **90**, 509–529.

——, R. A. Weller and R. Pinkel, 1986: Diurnal cycling: Observations and models of the upper-ocean response to diurnal heating, cooling, and wind mixing. *J. Geophys. Res.*, **91**, 8411–8427.

Schlichting, H., 1979: *Boundary Layer Theory.* McGraw-Hill.

Thompson, R. O. R. Y., 1973: Stratified Ekman boundary layer models. *Geophys. Fluid Dyn.*, **5**, 201–210.

Thorpe, S. A., 1987: Current and temperature variability on the continental slope. *Phil. Trans. Roy. Soc. London,* **A323**, 471–517.

Weatherly, G. L., 1975: A numerical study of time-dependent turbulent Ekman layers over horizontal and sloping bottoms. *J. Phys. Oceanogr.*, **5**, 288–299.

——, and P. P. Niiler, 1974: Bottom homogeneous layers in the Florida current. *Geophys. Res. Lett.*, **1**, 316–319.

——, and P. J. Martin, 1978: On the structure and dynamics of the oceanic bottom boundary layer. *J. Phys. Oceanogr.*, **8**, 557–570.

Zilitinkevich, S. S., 1972: On the determination of the height of the Ekman boundary layer. *Bound.-Layer Meteor.*, **3**, 141–145.